Acta Polytechnica **64**(4):350–359, 2024
https://doi.org/10.14311/AP.2024.64.0350

Published by the Czech Technical University in Prague

EXPERIMENTAL INVESTIGATION OF AN ENTROPY PRODUCTION IN A LINEAR BLADE CASCADE

Erik Flídr

Czech Aerospace Research Centre, Laboratory of High-Speed Aerodynamics, Beranových 130, 199 00 Prague, Czech Republic

correspondence: flidr@vzlu.cz

Abstract. The vortical structures in turbomachinery are crucial phenomena that significantly impact the machine's efficiency. Therefore, investigating them is essential for a better understanding of the machine's operation.

The presented paper focuses on an experimental investigation of entropy production in a linear blade cascade composed of prismatic blades for two pitch-to-chord ratios, $t/c = 0.6$, and 0.9. The effects of the inlet flow angle, $\alpha_1 = -20°,\ 5°,\ 30°$, and outlet isentropic Reynolds number, $Re_{2,\mathrm{is}} = (0.8,\ 1.2,\ 2.5,$ and $4.5) \times 10^5$, are examined based on pressure measurements.

Entropy production is evaluated as a balance of fluxes through the inlet and outlet boundaries of the control volume. The paper provides a detailed discussion of the local distribution of entropy production and vorticity in the flow field, as well as their evolution with the tested parameters. The correlations between the integral values of entropy production and the tested parameters are also given.

Keywords: Entropy production, linear blade cascade, experimental research.

1. Introduction

To the author's knowledge, Einstein's pioneering work [1] was the first present the evolution of secondary vorticity based on physical explanations. Since then, several authors have studied this phenomenon theoretically, for example, [2–9] or [10]. Initially, theoretical analysis required the curvature of the flow path and viscous fluid flow for the generation of vorticity, as shown by Dean [2]. Hawthorne [3] took a different approach, using fluid kinematics to derive the generation of secondary vorticity in curved channels. Subsequent work by Hawtrhone [4] connected theoretical descriptions with blade cascades in a simple manner.

Marris's work showed that the curvature of the flow path is not necessary for secondary vorticity generation (see [5]). Even a rotating reference frame has been studied in [8]. Lastly, intrinsic coordinates were used to describe this phenomenon in [10], where the impact of the individual terms in the Navier-Stokes equation on secondary vorticity was analysed, even for compressible fluids. The important results of these works for this study can be summarised as follows: Viscous forces are connected with the generation of vorticity in fluid flow in the end-wall boundary layers. This vorticity is then responsible for the generation of secondary vorticity in the curved channels and in their corners. The more curved the channel, the higher the centrifugal forces acting in the fluid, and therefore, stronger secondary vorticity is expected. Another parameter is the Reynolds number that causes vortex diffusion, and consequently different velocity gradients.

Although the theoretical description is powerful, the full picture of the vortices in blade cascades is beyond the capability of theoretical predictions. The separation of the inlet boundary layer in front of the cascade was observed in [11] as a place where the pressure at the end wall reached its maximal value. In this place, the so-called horseshoe vortex formed. Based on this experimental data, Langston in [12] formulated his secondary flow model, which was then modified several times, see e.g. [13], where the wrapping of the vortices was observed. Later, in [14], a more detailed model developed based on smoke visualisation experiments was presented. Several unknown vortices were found, and their interactions were studied in the cascade. This research resulted in defining the newest secondary flow model (according to the author's knowledge).

The flow through a linear blade cascade is affected by many variables.

The ideal case, when the blade worked under design conditions, was investigated by [15] and by [16]. The main goal of these works was to investigate the effect of the inlet boundary layer on the development of the secondary flow at the cascade outlet at different distances from the trailing edges of the blades. It has been shown that with increasing distance from the trailing edges, vortical structures migrate from the end wall towards the blade midspan. The effect of the inlet boundary layer on the secondary flow was as follows: With a thicker inlet boundary layer, stronger vortical structures are generated, and as a consequence, the kinetic energy dissipation at the cascade outlet is larger. The effects of the blade geometry and the state of the inlet boundary layer were investigated in [17]. This topic was studied in [18] from the unsteady point of view, where the evolution of Reynolds stress at the cascade outlet was measured at several positions

and the mixing of wake with vortical structures was described.

The effect of the inlet flow angle was investigated in [19–21], where the increasing inlet flow angle resulted in stronger vortical structures and their shifting towards the blade mid-span due to the larger centrifugal forces. Variation of Reynolds number and its impact on the flow were explored as well in [19, 21]. It was shown in [18] that with increasing Mach number, the secondary losses decreased significantly. This can be explained by the increasing ratio of inertial to centrifugal forces in the cascade, where the inertial forces acted against the generation of vortical structures. Moreover, the interaction between the vortical structures and the shock waves affected the results in the cases where the wave was present.

The comprehensive review of the topic was then published in [22] and more recently the newer findings were summarised in [23].

Note that the theoretical works focused on the mechanisms responsible for the generation of the vortical structures, and experimental works cited above focused on the evaluation of the dissipation of kinetic energy in the cascades. Although there are some papers where the entropy production in the cascade has been mentioned, see e.g. [24, 25], a comprehensive study of the entropy production due to the vortical structures in the blade cascade has, to the best of the authors' knowledge, not yet been carried out. Therefore, this work aims to perform this type of research to fill such a gap in the present literature.

2. Experimental apparatus, setup, and methods

2.1. Apparatus

2.1.1. Wind tunnel

The experiments were conducted in the VZLU Laboratory of High-Speed Aerodynamics, using a low-pressure, closed-loop wind tunnel (WT). The airflow was driven by a twelve-stage radial compressor, propelled by a 1.3 MW electric DC motor. The Mach number and Reynolds number can be set independently. Mach number can be changed by the rotational speed of the compressor, while the Reynolds number can be set by the change of the pressure in the tunnel by a set of vacuum pumps. To reduce air humidity, a condensation dryer was positioned behind the compressor, followed by a settling chamber in front of the test section. The latter was equipped with a screen to minimise fluctuation components of the velocity.

At the test section inlet, a pair of semi-shaped nozzles was placed in front of the cascade, determining the inlet flow angle. The cascade itself was mounted between two acrylic windows within the WT. The test section's width was 100 mm. Two tailboards were positioned behind the first and the last blade of the cascade. The pressure in the WT was regulated by a set of vacuum pumps located at the cascade outlet.

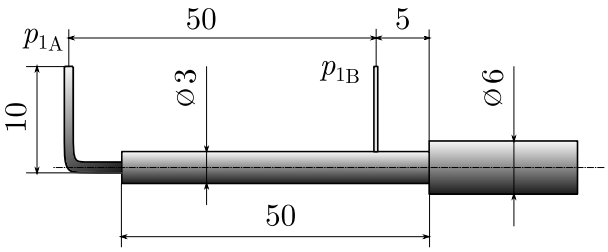

(A). Preston probe used for the measurement of the inlet flow field.

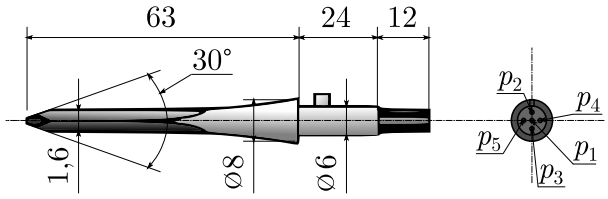

(B). Pyramid five-hole pressure probe.

Figure 1. Pressure probes.

2.1.2. Pressure probes

The inlet flow field was measured using the Preston probe positioned 30 mm upstream of the cascade, with the outer diameter of the pressure tap $d_\mathrm{p} = 0.4$ mm and a ratio of inner to outer diameter of the probe $d/d_\mathrm{p} = 0.5$. The probe was designed to measure the entire inlet flow field and was equipped with two identical pressure taps, as shown in Figure 1a.

The outlet flow field was measured by the pyramid five-hole pressure probe positioned 10 mm behind the cascade. The probe was manufactured from the tubes of the same diameter as the Preston tube, i.e. $d_\mathrm{p} = 0.4$ with a ratio of $d/d_\mathrm{p} = 0.5$. The geometry of the probe is shown in Figure 1b.

2.1.3. Blade cascade

Two cascade configurations defined by different pitch to chord ratios ($t/c = 0.6$ and 0.9), were investigated. These pitches modelled both the hub and tip sections of the real turbine wheel of the high-pressure part of the machine. The cascade schematic, including the definition of a coordinate system and the entire control volume, is shown in Figure 2. The cascades were assembled from prismatic blades with the same geometry for both configurations. Individual blades were assembled between two acrylic WT windows. The blade chord was $c = 50$ mm, the axial chord was $c_\mathrm{ax} = 36$ mm, and the blade height was the same as the width of the WT test section, i.e. $h = 100$ mm. The thickness of the blade trailing edges was $\varepsilon = 1$ mm. The periodicity of the flow was ensured by a large number of blades in cascades (11 for $t/c = 0.9$ and 14 for $t/c = 0.6$) and by the presence of tailboards.

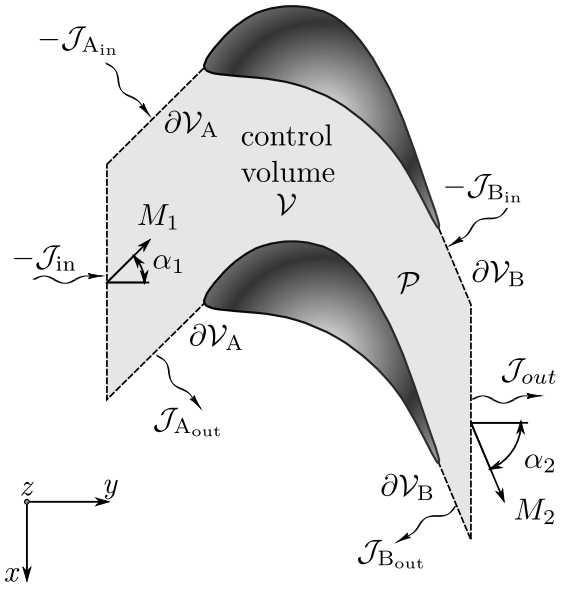

Figure 2. Control volume, with the cascade coordinate system definition.

2.1.4. Data acquisition and measurement uncertainty

Individual pressure signals were measured by the differential pressure transducers Druck with a reading accuracy of 0.1 % (rdg). These analogue voltage signals were then conditioned by the DEWETRON system and sampled by the A/D card (National Instruments PCI-6259 A/D card: 16-Bit, 1 MS s^{-1} (Multichannel), 1.25 MS s^{-1} (1-Channel), 32 Analogue Inputs). One measured point takes 3 seconds with a sampling rate of 1000 Hz. The low-pass filter of 100 Hz was used. The obtained data were then averaged.

The barometric pressure was measured by the Druck DPI 145 digital pressure transducer with the precision of $p_{\mathrm{b}} = (p_{\mathrm{b}} \pm 15)$ Pa.

The stagnation temperature, as well as air humidity, was measured at the settling chamber by means of Sensorika Humistar HTP-1 hygrometer with accuracy $T = T \pm 0.3$ K and $RH = RH \pm 2$ %.

Uncertainties of measured quantities were evaluated with respect to the measurement chain and according to [26]. The outlet isentropic Mach number was set with the uncertainty of $M_{2,\mathrm{is}} = 0.40 \pm 0.01$. The outlet isentropic Reynolds number was set with the uncertainty of $Re_{2,\mathrm{is}} = (4.500 \pm 0.225) \times 10^5$. Local entropy production was then evaluated with the uncertainty of $\mathsf{p} = (132.134 \pm 21.046)$ J (K s m^2)$^{-1}$. Note, that all of these values represent the worst cases. Uncertainties were based on 95 % confidence level (± 2 standard deviation).

2.2. Setup

2.2.1. Inlet flow field measurement

The inlet flow fields were measured for constant inlet flow angle $\alpha_1 = 5°$ because the inlet boundary layers were insensitive to the variation of this parameter. The measurements were performed for four levels of isentropic Reynolds number ($Re_{\mathrm{is}} = (0.80,\ 1.25,\ 2.50$ and $4.50) \times 10^5$) and for a constant value of outlet isentropic Mach number $M_{2,\mathrm{is}} = 0.4$. The inlet boundary layers were then measured at three positions z (at the blade channel centre and in front of the leading edges of the neighboring blades) to provide a better understanding of the inlet flow field. These measurements were subsequently averaged.

2.2.2. Outlet flow field measurement

The outlet flow fields were measured for the same values of isentropic Reynolds number and Mach number as in the case of the inlet flow fields. The effect of the inlet flow angle was studied for $\alpha_1 = -20°,\ 5°$ and $30°$, with nominal inlet flow angle $\alpha_1 = 5°$.

2.3. Used methods

The air was considered a perfect gas, and heat transfer was not taken into account; thus, an adiabatic flow approach was used to evaluate the measured data.

2.3.1. Measurements in the Shear Flow and the Boundary Layers

Measurements with the pressure probes in shear flows and close to the wall were corrected for the virtual shift of the probe position and blockage effects. The correction for the probe positions, originally proposed by [27] and later modified by [28], was extended in a subsequent work by [29]. This final correction was employed in the following form:

$$\Delta z = \epsilon d_{\mathrm{p}} = 0.15 \tanh\left(4\sqrt{\beta}\right) - \epsilon_{\mathrm{w}}, \tag{1}$$

where

$$\epsilon_{\mathrm{w}} = \mathcal{A}\left(\frac{z}{d_{\mathrm{p}}} - 3\right) + \mathcal{B}\left(\frac{z}{d_{\mathrm{p}}} - 3\right)\left[0.15 \tanh\left(4\sqrt{\beta}\right)\right], \tag{2}$$

and where:

$$\beta = \frac{d_{\mathrm{p}}}{2u}\frac{\mathrm{d}u}{\mathrm{d}z}. \tag{3}$$

Here, u is the velocity and $\mathcal{A} = 0.174$ and $\mathcal{B} = -1.25$ are constants. Near wall correction was used up to $y/\delta = 3$, as was suggested by [29].

2.3.2. Outlet flow field evaluation

The velocity vector field was obtained from the measured pressures thanks to the calibration of the five-hole pressure probe. The y components of the vorticity vector were then directly calculated from the velocity as:

$$\omega_y = \frac{u_x^{(i+1),j} - u_x^{(i-1),j}}{z^{(i+1),j} - z^{(i-1),j}} - \frac{u_z^{i,(j+1)} - u_z^{i,(j-1)}}{x^{i,(j+1)} - x^{i,(j-1)}}, \tag{4}$$

where u_x and u_z are the velocity components in the x and z direction, respectively. The rest of the components of the vorticity vector were calculated from Crocco's theorem written in the form:

$$\epsilon_{ijk} u_j \omega_k = \frac{1}{\varrho}\partial_i p_0, \tag{5}$$

t/c	$Re_{2,\mathrm{is}} \times 10^{-5}$	$Re_{\mathrm{y}} \times 10^{-5}$	δ^* [mm]	θ [mm]	$H_{1,2}$
0.6	4.50	13.2	1.3	0.5	2.43
	2.50	7.4	1.0	0.4	2.32
	1.25	3.5	0.7	0.5	1.35
	0.80	2.6	0.5	0.4	1.42
0.9	4.50	14.8	1.2	0.5	2.51
	2.50	8.3	1.0	0.4	2.48
	1.25	4.1	0.8	0.6	1.32
	0.80	2.7	0.7	0.5	1.43

TABLE 1. Inlet boundary layers parameters

where ϵ_{ijk} is the Levi-Civita alternating tensor and p_0 is the stagnation pressure. The local distribution of the entropy production is obtained as a difference between the entropy flux through the inlet and outlet control volume boundaries:

$$\mathsf{p} = \mathcal{J}_{\mathrm{out}} - \mathcal{J}_{\mathrm{in}} = \varrho_2 u_{2_{\mathrm{y}}} s_2 - \varrho_1 u_{1_{\mathrm{y}}} s_1, \tag{6}$$

where s stands for the entropy and ϱ is the fluid density. The density upstream of the cascade was considered constant, as the flow Mach number was lower than $M < 0.09$. However, at the cascade outlet, the flow Mach number was $M_{2,\mathrm{is}} = 0.4$. Therefore, the density distribution was calculated at individual measurement points using the perfect gas law and known static pressure and temperature. Note, that the fluxes across the boundaries $\partial\mathcal{A}$ and $\partial\mathcal{B}$ give no contribution to the entropy production thanks to the periodic boundary conditions.

The averaged outlet flow field was evaluated based on the data reduction method briefly described in [21]. The averaged entropy productions in the individual z positions were evaluated as:

$$\langle \mathsf{p} \rangle = \langle \mathcal{J}_{\mathrm{out}} \rangle - \mathcal{J}_{\mathrm{in}} = \langle \varrho_2 \rangle \langle u_{2_{\mathrm{y}}} \rangle \langle s_2 \rangle - \varrho_1 u_{1_{\mathrm{y}}} s_1. \tag{7}$$

Supposing the superposition of the two-dimensional flow at the cascade mid-span ($z = h/2$) and the end-wall flows, the entropy production caused by these end-wall flows was obtained as:

$$\langle \mathsf{p}_{\mathrm{ew}} \rangle_z = \frac{\langle \mathsf{p} \rangle_z}{\langle \mathsf{p} \rangle_{z=\frac{h}{2}}}. \tag{8}$$

The total entropy production in the outlet flow field was then obtained by integration over the entire cascade outlet:

$$\mathcal{P} = \frac{h}{2t} \int_0^{h/2} \int_0^{2t} \mathsf{p} \mathrm{d}x \mathrm{d}z, \tag{9}$$

where t stands for the blade pitch. The overall entropy production in the end-wall region was calculated as:

$$\mathcal{P}_{\mathrm{nw}} = \mathcal{P} - \mathcal{P}_{\mathrm{ms}}. \tag{10}$$

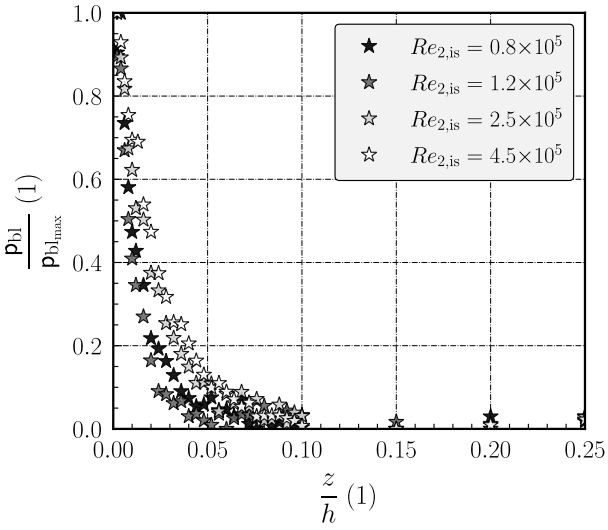

FIGURE 3. Normalised Local distribution of the entropy production for $t/c = 0.9$.

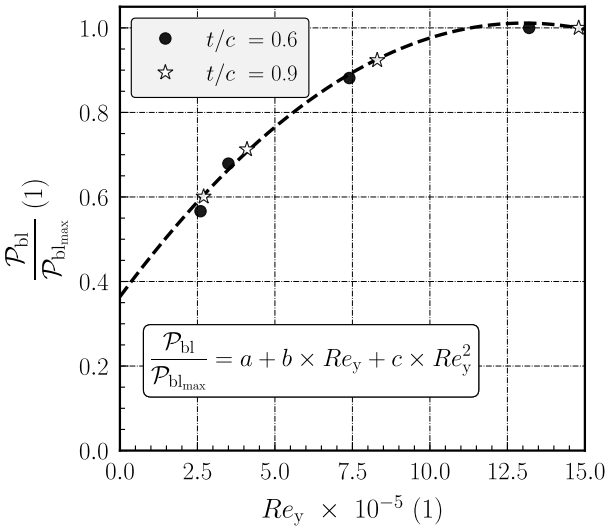

FIGURE 4. Integral entropy production for both studied cascades.

3. Results and discussion

3.1. Inlet flow field

The inlet flow field was investigated in detail in [30]. It was found that the inlet boundary layers behaved as boundary layers evolved on the flat plate and were laminar for $Re_{2,\mathrm{is}} = (0.8 \text{ and } 1.2) \times 10^5$ and turbulent for $Re_{2,\mathrm{is}} = (2.5 \text{ and } 4.5) \times 10^5$. The parameters of the inlet boundary layers are summarised in Table 1.

Normalised local distribution of the entropy production across the WT test section for $t/c = 0.9$ is shown in Figure 3 and normalised integral values of the entropy productions for all studied cases are then given in Figure 4. The normalisation was performed using the maximal value of entropy production obtained from all tested cases.

As expected, an increase in Reynolds number led to a higher entropy production in the inlet boundary layers, attributed to the growing boundary layer

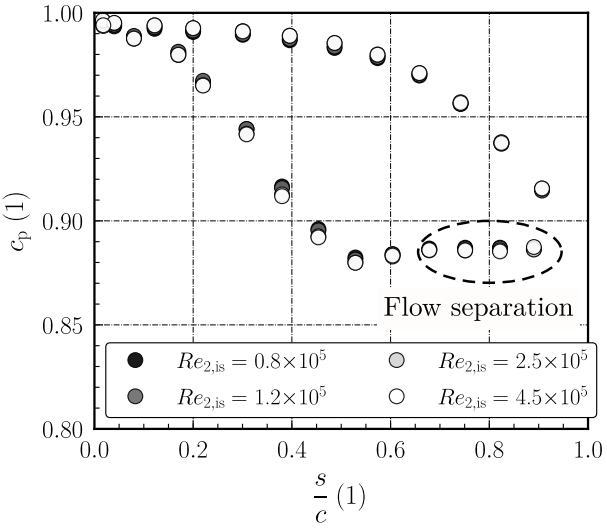

Figure 5. Pressure coefficient distribution for $t/c = 0.6$ and $\alpha_1 = 5°$.

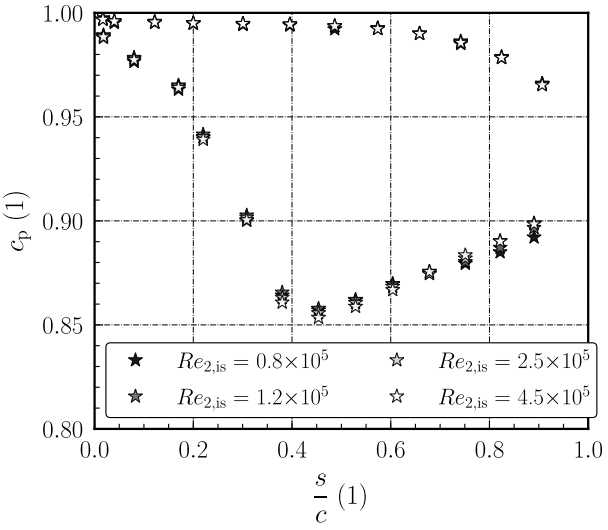

Figure 6. Pressure coefficient distribution for $t/c = 0.9$ and $\alpha_1 = 5°$.

thickness. Moreover, in the turbulent boundary layers, higher velocity gradients were observed in this region.

The dependency of the integral entropy production on the Reynolds number Re_y was approximated by the second order polynomial function with coefficients: $a = 0.3640$, $b = 0.0993$, and $c = -0.0038$. These data suggest a potential universal relationship between the entropy production in the boundary layer on a flat plate and Reynolds number Re_y, a topic to be investigated in future studies.

This basic evaluation of the inlet flow field gave the inlet boundary condition for the calculation of the balance Equation (6).

3.2. Blade pressure distribution

Figure 5 illustrates an example of the pressure coefficient distribution on the blade surfaces for $t/c = 0.6$ with the nominal inlet flow angle. Flow separation became evident from $s/c \approx 0.65$ up to the trailing edge of the blade. While this phenomenon was consistently observed for all tested inlet flow angles of the cascade with a pitch-to-chord ratio $t/c = 0.6$, it was not found in the other tested cascade with $t/c = 0.9$. This result will be further discussed in Section 3.3.

The distribution of the pressure coefficient on the blade surface for $t/c = 0.9$ is depicted in Figure 6. Surprisingly, no separation occurred in this case, despite the larger diffusion factor for this pitch-to-chord ratio.

3.3. Outlet flow field

3.3.1. Local entropy production

To illustrate the local distribution of entropy production at the cascade outlet for the tested case $t/c = 0.9$, inlet flow angle $\alpha_1 = 30°$, and Reynolds number $Re_{2,is} = 2.5 \times 10^5$, refer to Figure 7. The contour lines depict the distribution of the streamwise vorticity, while the colours illustrate the normalised local entropy production[1]. Individual vortices were identified and highlighted behind one blade. Wakes are evident at the cascade midspan, where the entropy generation is higher. However, the majority of the entropy is generated in the endwall region between the individual vortices. This

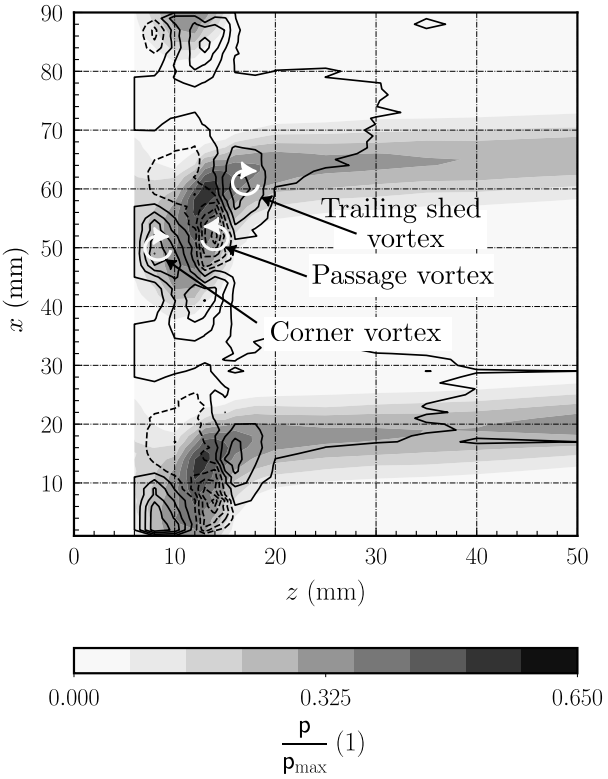

Figure 7. Distribution of the normalised local entropy production at the cascade outlet with contours of the vorticity for $t/c = 0.9$, $\alpha_1 = 30°$, and $Re_{2,is} = 2.5 \times 10^5$.

[1]The highest value of local entropy production from all tested cases was taken as the normalisation factor. Since the presented case did not reach this extreme, the value $p = 1$ is not included in Figure 7.

observation is attributed to the highest velocity gradients in this region, as evident from the entropy production equation (the derivation is provided in [31] or, in general curvilinear coordinates, in [32]):

$$\mathsf{p} = -\partial_i p + \lambda \left(\partial_i u_i\right)^2 + 2\mu \partial_i u_j \partial_j u_i, \qquad (11)$$

where the pressure gradients as well as the compressibility effects represented by the velocity divergence were negligible compared to velocity gradients.

3.3.2. Averaged entropy production caused by the end-wall flows

Averaged entropy productions for different inlet flow angles and the cascade configuration $t/c = 0.9$ are presented in Figures 8–10. These values were normalised by the entropy production at the cascade mid-span to assess the impact of the end-wall flows. It is important to note that, in the case of $\alpha_1 = -20°$, entropy production peaks were not identified due to their occurrence in regions where the probe was unable to perform measurements.

The increase in the inlet flow angle resulted in the shift of the entropy production peak from the end-wall region towards the blade midspan, from the precisely unknown position for $\alpha_1 = -20°$ up to $z/h \approx 0.12$ for $\alpha_1 = 30°$. This is caused by the larger centrifugal forces acting in the cascade due to the higher flow turning. This larger force generates the higher secondary vorticity in the blade channel, as was theoretically shown by [4], which moves with the vortices. In addition, there is also a clear increase in the entropy production with increasing α_1. The reason for this observation is the same as for the peak shift, i.e., the higher centrifugal forces that are responsible for the generation of the stronger vortices.

Focusing on the evolution with Reynolds number shows that with increasing $Re_{2,\mathrm{is}}$, the entropy production grows as well. This is caused by the topology of the vortical structures. The higher inertial forces were responsible for smaller vortices diffusion, therefore, larger velocity gradients occurred between the vortices, which is in agreement with the theoretical prediction of Equation (11).

3.3.3. Integral entropy production in the blade cascade

Figure 11 shows the normalised integral entropy productions for both studied cases as a function of Reynolds number. The maximal value of the entropy production from all cases was chosen to normalise the evaluated data. It can be concluded, that the maximum entropy was observed for the case with $t/c = 0.6$, $\alpha_1 = 30°$, and $Re_{2,\mathrm{is}} = 4.5 \times 10^5$. The occurrence of maximum entropy in this case was expected. The small differences between individual cases on this pitch-to-chord ratio $t/c = 0.6$ were interesting and not expected. These little variances were caused

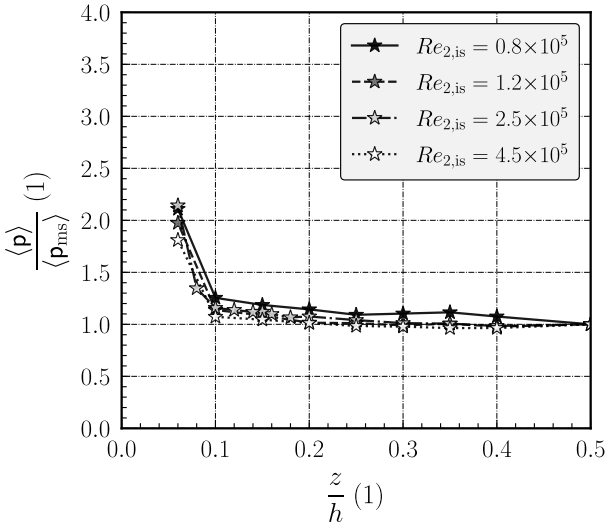

FIGURE 8. Averaged normalised entropy production in the end-wall region for $t/c = 0.9$ and $\alpha_1 = -20°$.

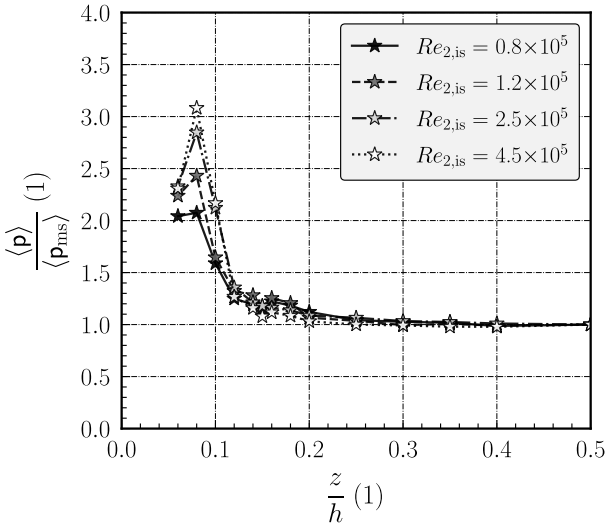

FIGURE 9. Averaged normalised entropy production in the end-wall region for $t/c = 0.9$ and $\alpha_1 = 5°$.

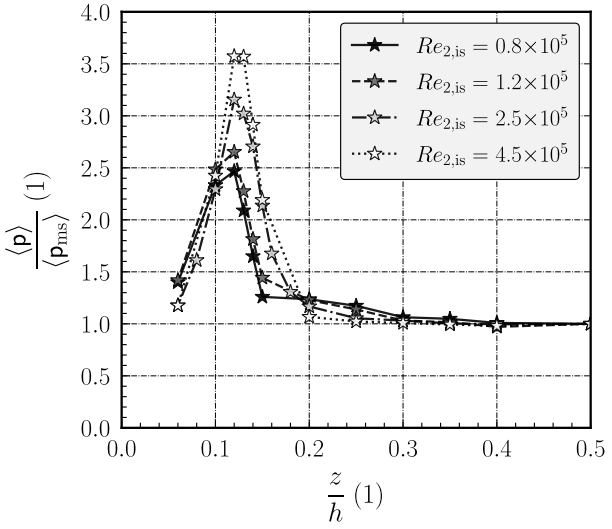

FIGURE 10. Averaged normalised entropy production in the end-wall region for $t/c = 0.9$ and $\alpha_1 = 30°$.

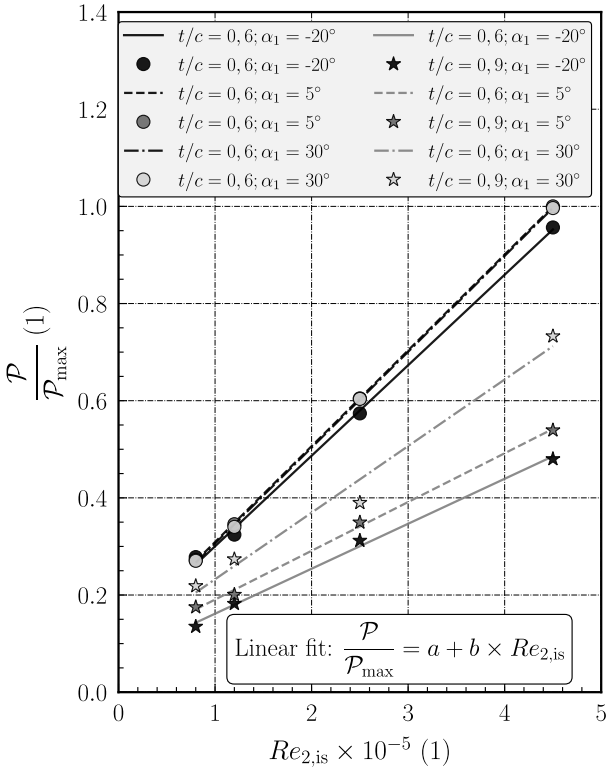

Figure 11. Integral entropy production for both tested cases plotted as a function of Reynolds number.

Cascade t/c	a	$b \times 10^5$
	0.114	0.186
0.6	0.112	0.197
	0.109	0.197
	0.069	0.093
0.9	0.090	0.100
	0.095	0.137

Table 2. Constants for approximation of integral entropy production in linear blade cascade.

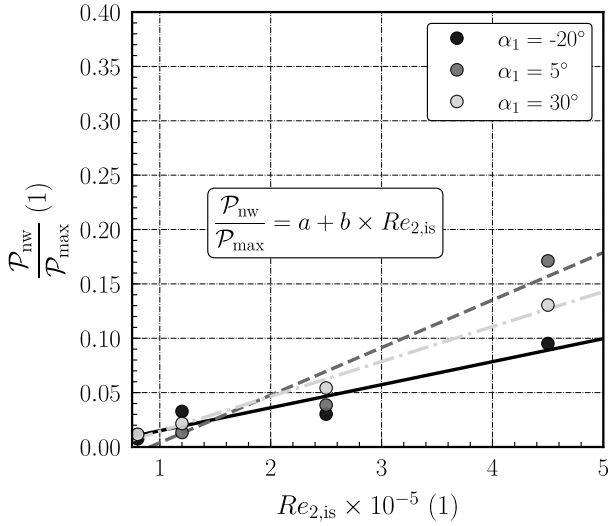

(a). Normalised near-wall entropy production for $t/c = 0.6$.

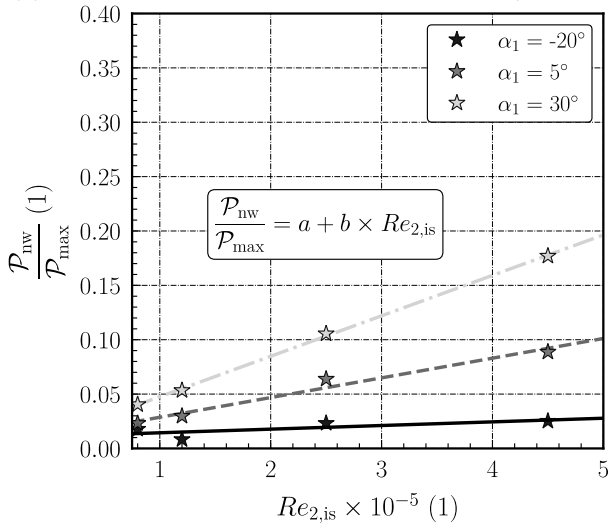

(b). Normalised near-wall entropy production for $t/c = 0.9$.

Figure 12. Normalised near-wall entropy production.

by the boundary layer separation on the suction surfaces for all studied inlet flow angles. The majority of the entropy was generated in the separation region, overshadowing the effects of vortices in the end wall region.

Significant variations between individual inlet flow angles were observed in the case of $t/c = 0.9$, where entropy production increases with increasing α_1. Entropy production for this case was considerably lower compared to the case of $t/c = 0.6$.

In general, a linear dependency between the entropy production and this similarity criterion exists within the studied range of Reynolds numbers. The correlation parameters for the linear fits are summarised in Table 2. The normalised entropy production caused by vortical structures in the blade cascades was evaluated using Equation (10). Specifically, the mid-span value of the overall entropy production was subtracted and then divided by the maximal entropy production from all tested cases. Results of this approach are plotted in Figures 12a and 12b, respectively. First-order polynomial functions were used to approximate the data for all cases under investigation. The coefficients obtained from these approximations are summarided in Table 3. In both cases, the entropy production associated with vortical structures increased similarly with the Reynolds number. In the case of the cascade configuration with $t/c = 0.6$, the effect of the inlet flow angle on the entropy production was influenced by flow separation, as is evident from the points in Figure 12a. In this case, the data could not be approximated as effectively (using a linear approximation) compared to the other tested cascades, primarily due to the frequently mentioned flow separation. The interaction of the vortical structures with this separation caused that the assumption about the superposition of the 2D flow at the blade mid-span and the end wall flow was not quite right.

Cascade t/c	a	b
	−0.006	0.021
0.6	−0.0398	0.0437
	−0.0178	0.0321
	0.0111	0.0033
0.9	0.0106	0.0181
	0.0104	0.0372

TABLE 3. Coefficients for approximation of near-wall entropy production in linear blade cascade.

4. CONCLUSION

The experimental research on entropy production in a linear blade cascade was conducted for two different pitch-to-chord ratios under a constant outlet isentropic Mach number of 0.4. The study involved four different levels of Reynolds number $(0.8,\ 1.2,\ 2.5,\ \text{and}\ 4.5) \times 10^5$ and three inlet flow angles: −20°, 5°, and 30°.

The inlet entropy flux was assessed as the boundary condition at the inlet. It was demonstrated that a correlation exists between the entropy production in the boundary layer and the Reynolds number, modelled by a second-order polynomial function.

The local distribution of parameters in the outlet flow field revealed the relationship between the positions of the vortices and entropy production. The majority of entropy production took place between the vortices, where the velocity gradients were the largest.

Increasing the inlet flow angle intensified the vortical structures and caused their shift from the end wall towards the blade mid-span, driven by the larger centrifugal forces resulting from the higher flow turning.

While the variation in Reynolds number did not significantly impact the distribution of vortical structures and entropy production, an increase in Reynolds number led to the magnification of entropy production. This effect resulted from less diffused vortical structures, leading to larger velocity gradients within the individual vortices and between them.

The pitch-to-chord ratio affected both the distribution and strength of the vortical structures, as well as the amount of entropy production. For $t/c = 0.6$, the vortices were more shifted toward the blade mid-span and exhibited greater strength due to the larger centrifugal forces, resulting from the narrower channel.

Finally, correlations were established between the overall entropy productions in the outlet flow field, as well as the relationships between the entropy production caused by the vortical structures and Reynolds number. These correlations take the form of first-order polynomial functions.

Future work should focus on investigating the effects of flow separation on the suction side of the blade and its impact on the data evaluation procedure. It has been demonstrated that in cases where the separation did not occur ($t/c = 0.9$), the assumption of superposition of the 2D flow at the blade midspan and the vortical motion in the end wall region is valid. However, in cases where separation occurred ($t/c = 0.6$), this approach was not entirely appropriate for the evaluation. Therefore, a more suitable method should be developed to ensure an accurate data evaluation.

LIST OF SYMBOLS

$\mathcal{A}$, $\mathcal{B}$ empirical constants
c blade chord [mm]
c_{ax} axial blade chord [mm]
c_{p} pressure coefficient
d probe diameter
h blade height [mm]
$H_{1,2}$ shape parameter
$\mathcal{J}$ flux through the boundary of the control volume
M Mach number
p pressure
p local entropy production
$\mathcal{P}$ integral entropy production
Re Reynolds number
t cascade pitch [mm]
u flow velocity $[\mathrm{m\,s^{-1}}]$
$\mathcal{V}$ control volume $[\mathrm{m^3}]$
$x,\ y,\ z$ Cartesian coordinates [m]
α inlet flow angle [°]
δ^* displacement boundary layer thickness [mm]
ε trailing edge thickness [mm]
θ momentum boundary layer thickness [mm]
$\langle\bullet\rangle$ averaged parameter
rdg reading value
fs full scale

Subscripts:

1 cascade inlet
2 cascade outlet
b barometric
ew cascade end-wall
is isentropic
ms mid-span
nw end-wall
x, y, z in the circumferential, axial, and radial directions

ACKNOWLEDGEMENTS

The work was not supported by any project, only by the author's curiosity.

Declaration:
The spell check for this paper was conducted using ChatGPT 3.5.

REFERENCES

[1] C. Yogananda, A. Einstein. The cause of the formation of meanders in the courses of rivers and of the so-called Baer's law. *Resonance* **5**:105–108, 2000. https://doi.org/10.1007/BF02839006

[2] W. Dean. XVI. Note on the motion of fluid in a curved pipe. *The London, Edinburgh, and Dublin Philosophical Magazine and Journal of Science* **4**(20):208–223, 1927. https://doi.org/10.1080/14786440708564324

[3] W. R. Hawthorne. Secondary circulation in fluid flow. *Proceedings of the Royal Society of London Series A Mathematical and Physical Sciences* **206**(1086):374–387, 1951. https://doi.org/10.1098/rspa.1951.0076

[4] W. R. Hawthorne. Rotational flow through cascades part I – The components of vorticity. *The Quarterly Journal of Mechanics and Applied Mathematics* **8**(3):266–279, 1955. https://doi.org/10.1093/qjmam/8.3.266

[5] A. W. Marris. The generation of secondary vorticity in an incompressible fluid. *Journal of Applied Mechanics* **30**(4):525–531, 1963. https://doi.org/10.1115/1.3636613

[6] A. W. Marris. On the generation of secondary velocity along a vortex line. *Journal of Basic Engineering* **86**(4):815–818, 1964. https://doi.org/10.1115/1.3655961

[7] A. W. Marris. Generation of secondary vorticity in a stratified fluid. *Journal of Fluid Mechanics* **20**(2):177–181, 1964. https://doi.org/10.1017/S0022112064001124

[8] A. W. Marris. Secondary flows in an incompressible fluid of varying density in a rotating reference frame. *Journal of Basic Engineering* **88**(2):533–537, 1966. https://doi.org/10.1115/1.3645894

[9] A. W. Marris, S. L. Passman. Vector fields and flows on developable surfaces. *Archive for Rational Mechanics and Analysis* **32**(1):29–86, 1969. https://doi.org/10.1007/BF00253256

[10] B. Lakshminarayana, J. H. Horlock. Generalized expressions for secondary vorticity using intrinsic co-ordinates. *Journal of Fluid Mechanics* **59**(1):97–115, 1973. https://doi.org/10.1017/S0022112073001448

[11] L. S. Langston, M. L. Nice, R. M. Hooper. Three-dimensional flow within a turbine cascade passage. *Journal of Engineering for Power* **99**(1):21–28, 1977. https://doi.org/10.1115/1.3446247

[12] L. S. Langston. Crossflows in a turbine cascade passage. *Journal of Engineering for Power* **102**(4):866–874, 1980. https://doi.org/10.1115/1.3230352

[13] C. H. Sieverding, P. Van den Bosche. The use of coloured smoke to visualize secondary flows in a turbine-blade cascade. *Journal of Fluid Mechanics* **134**:85–89, 1983. https://doi.org/10.1017/S0022112083003237

[14] H. P. Wang, S. J. Olson, R. J. Goldstein, E. R. G. Eckert. Flow visualization in a linear turbine cascade of high performance turbine blades. *Journal of Turbomachinery* **119**(1):1–8, 1997. https://doi.org/10.1115/1.2841006

[15] H. P. Hodson, R. G. Dominy. The off-design performance of a low-pressure turbine cascade. *Journal of Turbomachinery* **109**(2):201–209, 1987. https://doi.org/10.1115/1.3262086

[16] L. Chen, S. L. Dixon. Growth of secondary flow losses downstream of a turbine blade cascade. In *Proceedings of the ASME 1985 Beijing International Gas Turbine Symposium and Exposition*, vol. 1. 1985. https://doi.org/10.1115/85-IGT-35

[17] E. Rosa de la Blanco, H. P. Hodson, R. Vazquez, D. Torre. Influence of the state of the inlet endwall boundary layer on the interaction between pressure surface separation and endwall flows. In *Proceedings of the Institution of Mechanical Engineers, Part A: Journal of Power and Energy*, vol. 217, pp. 433–441. 2003. https://doi.org/10.1243/095765003322315496

[18] A. Perdichizzi, M. Ubaldi, P. Zunino. Reynolds stress distribution downstream of a turbine cascade. *Experimental Thermal and Fluid Science* **5**(3):338–350, 1992. https://doi.org/10.1016/0894-1777(92)90079-K

[19] H. P. Hodson, R. G. Dominy. Three-dimensional flow in a low-pressure turbine cascade at its design condition. *Journal of Turbomachinery* **109**(2):177–185, 1987. https://doi.org/10.1115/1.3262083

[20] A. Perdichizzi, V. Dossena. Incidence angle and pitch–chord effects on secondary flows downstream of a turbine cascade. *Journal of Turbomachinery* **115**(3):383–391, 1993. https://doi.org/10.1115/1.2929265

[21] E. Flídr, T. Jelínek, M. Kladrubský. Experimental investigation of effects of Reynolds number and incidence angle on secondary flow within a linear blade cascade. *Journal of Thermal Science* **30**(6):2122–2136, 2021. https://doi.org/10.1007/s11630-021-1455-y

[22] C. H. Sieverding. Recent progress in the understanding of basic aspects of secondary flows in turbine blade passages. *Journal of Engineering for Gas Turbines and Power* **107**(2):248–257, 1985. https://doi.org/10.1115/1.3239704

[23] P. Ligrani, G. Potts, A. Fatemi. Endwall aerodynamic losses from turbine components within gas turbine engines. *Propulsion and Power Research* **6**(1):1–14, 2017. https://doi.org/10.1016/j.jppr.2017.01.006

[24] D. Šimurda, J. Fürst, J. Hála, et al. Near-wall flow in the blade cascades representing last rotor root section of large output steam turbines. *Journal of Thermal Science* **30**(1):220–230, 2021. https://doi.org/10.1007/s11630-020-1246-x

[25] D. Šimurda, J. Fürst, M. Luxa. 3D flow past transonic turbine cascade SE 1050 – Experimental and numerical simulations. *Journal of Thermal Science* **22**(4):311–319, 2013. https://doi.org/10.1007/s11630-013-0629-7

[26] GUM. *Guide to the expression of uncertainty in measurement (GUM)-Supplement 1: Numerical methods for the propagation of distributions.* International Organization for Standardization, (1995).

[27] F. A. MacMillan. Experiments on Pitot-tubes in shear flow. Tech. rep., Ministry of Supply, 1956.

[28] B. McKeon, J. Li, W. Jiang, et al. Pitot probe corrections in fully developed turbulent pipe flow. *Measurement Science and Technology* **14**(8):1449–1458, 2003. https://doi.org/10.1088/0957-0233/14/8/334

[29] S. C. C. Bailey, M. Hultmark, J. P. Monty, et al. Obtaining accurate mean velocity measurements in high Reynolds number turbulent boundary layers using Pitot tubes. *Journal of Fluid Mechanics* **715**:642–670, 2013. https://doi.org/10.1017/jfm.2012.538

[30] E. Flídr, T. Jelínek, M. Kladrubský. Boundary layer investigation at the inlet of a linear balde cascade. In *Topical Problems of Fluid Mechanics*, pp. 83–90. (2018). https://doi.org/10.14311/TPFM.2018.011

[31] P. Asinari, E. Chiavazzo. Overview of the entropy production of incompressible and compressible fluid dynamics. *Meccanica* **51**(5):1245–1255, 2016. https://doi.org/10.1007/s11012-015-0284-z

[32] E. Flídr. Derivation of entropy production in a fluid flow in a general curvilinear coordiante system. *Acta Polytechnica* **63**(2):103–110, 2023. https://doi.org/10.14311/AP.2023.63.0103